THE JOURNAL OF PHYSICAL CHEMISTRY C

Article

pubs.acs.org/JPCC

Double Perovskite Cs_2BBiX_6 (B = Ag, Cu; X = Br, Cl)/TiO_2 Heterojunction: An Efficient Pb-Free Perovskite Interface for Charge Extraction

Hong-Jian Feng,*[,†] Wan Deng,[†] Kang Yang,[†] Jinsong Huang,[‡] and Xiao Cheng Zeng*[,§,‡]

[†]School of Physics, Northwest University, Xi'an 710069, People's Republic of China

[‡]Department of Mechanical and Materials Engineering, University of Nebraska-Lincoln, Lincoln, Nebraska 68588, United States

[§]Department of Chemistry, University of Nebraska-Lincoln, Lincoln, Nebraska 68588, United States

Supporting Information

ABSTRACT: Motivated from the recent success in synthesizing bismuth-based double perovskites (*J. Am. Chem. Soc.* **2016**, *138*, 2138−2141), we perform a comprehensive study of interfacial properties of bismuth-based double perovskites Cs_2AgBiX_6 (X = Br, Cl) and TiO_2 interfaces. The bismuth-based double perovskites possess desirable electronic and optical properties as excellent light absorber and thus may serve as lead-free alternatives to the organic−inorganic perovskites. On the basis of density functional theory computation, we systematically study the Cs_2BBiX_6 (B = Ag, Cu; X = Br, Cl)/TiO_2 interfaces and analyze the trend of charge transfer across the interfaces. We find that the Cs_4X_4 (X = Br and Cl)/TiO_2-mediated interfaces are prospective interfaces for charge extraction and separation due largely to the withdrawn trap states for the TiO_2 part when in contact with the Cs_4X_4 termination. Moreover, the ionic interaction and charge redistribution across the specific interfaces can lead to the appropriate band alignment, reduced band gap for the rock-salt double perovskite part, and smooth gradient distribution for the locally projected density of states along the normal direction to the interfaces, further facilitating the charge transfer. Overall, we predict that bismuth-based double perovskites Cs_2AgBiX_6 (X = Br, Cl) and TiO_2 interfaces are highly efficient for charge extraction, suggesting high potential for interfacial engineering optoelectronic devices.

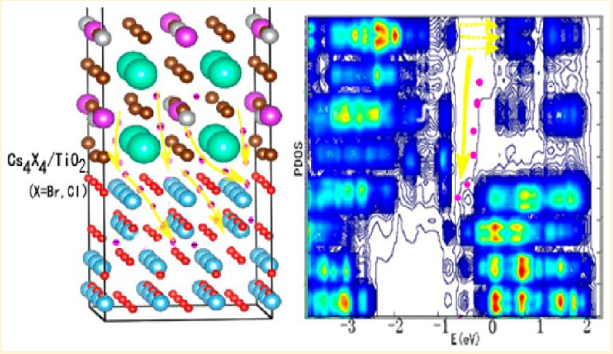

1. INTRODUCTION

Organometal halide hybrid perovskites, AMX_3 [A= $CH_3NH_3^+$, $HC(NH_2)_2^+$; M = Pb^{2+}, Sn^{2+}; X = Cl^-, Br^-, and I^-], have become highly interested materials for photovoltaic solar cells because of their excellent visible-light absorption,[1−4] long diffusion length for the photogenerated electron−hole pairs,[5−7] high carrier mobilities and lifetime,[8] as well as capability in recycling of the carriers within a relatively large area of the samples.[9,10] In particular, methylammonium lead trihalide perovskites possess a lower bound value of ∼10 $cm^2\ V^{-1}\ s^{-1}$ for the high-frequency charge mobility.[8] Even in polycrystalline thin films, the diffusion length can reach one micron, while the carrier lifetime can be longer than 1 μs.[11−13] The relatively long lifetime and modest carrier mobilities are likely attributed to the electron−phonon scattering of the carriers rather than the impurity or defect scattering.[12] Both features were proposed to be attributed to the strong polaron effect, owing to the interaction between the organic part and the trapped electrons.[14] The strong optical absorption is associated with the p orbital transition between halide ion 4p/5p and Pb^{2+} 6p states. Moreover, the conduction band minimum (CBM) is mainly contributed by the lead 6p states, while the valence band maximum (VBM) mainly stems from the halide p and lead 6s states. Although the physical mechanism underlying the visible-light absorption and carrier dynamics is partially understood, several critical issues still need to be resolved for wide applications of the perovskites in solar cells.

The first critical issue is to find alternatives to the toxic lead element in the organolead halide perovskites. Tin halide perovskites were considered as suitable candidates due to their desirable band gap. However, the tin counterparts are much less stable in air and not necessarily less toxic.[15−17] Photostability,[18−20] moisture stability,[21−28] and thermal stability[29−31] are other critical issues that prevent the organometal halide perovskites from commercialization. Recently, bismuth-based halide double perovskites, that is, Cs_2AgBiX_6 (X = Br, Cl), have been synthesized and have received increasing attention due to their potential in addressing some of the critical issues mentioned above[31−35] as lead-free perovskites. Snaith et al. suggested potential application of the double perovskites for

Received: January 6, 2017
Revised: February 8, 2017
Published: February 9, 2017

DOI: 10.1021/acs.jpcc.7b00138
J. Phys. Chem. C 2017, 121, 4471−4480

solar cells in view of the peculiar electronic properties of the perovskites as light absorber.[34] Besides desired optical band gap and visible-light absorption, their stabilities under light, humid environment, and heat are improved significantly compared with the organolead halide perovskites. Moreover, the bismuth-based halide double perovskites also exhibit very long carrier recombination lifetime of ca. 660 ns, as determined from the room-temperature time-resolved photoluminescence decay measurement. Exposure to light and humidity for 30 days and heating at 100 °C for 72 h did not show evidence of decomposition of the double perovskites. The high stability and the relatively long carrier lifetime render the double perovskites as good candidates for photovoltaic applications.

In typical perovskite solar cells, electron transport layer (ETL) like TiO_2[36,37] and hole transport layer (HTL) like spiro-MeOTAD [2,2′,7,7′-tetrakis (*N*,*N*-di-*p*-methox- yphenyl-amine)-9,9-spirobifluorene][38,39] are used to extract photo-induced electrons and holes toward the corresponding electrodes. Understanding the charge separation and the recombination mechanism at the interfaces of the solar cell devices is important to the design and fabrication of more efficient solar cells. On the basis of density functional theory (DFT) computations, we previously studied charge transport in AMX_3/TiO_2 heterojunctions and demonstrated that the charge accumulation at the interfaces and the interfacial structures determine the direction of charge transfer in the perovskite heterojunctions.[40,41] For consideration of the double perovskites like Cs_2AgBiX_6 (X = Br, Cl) as light absorber in solar cells, it is important to examine whether the Cs_2AgBiX_6 (X = Br, Cl) materials possess good charge extraction capability and band alignment with the TiO_2 ETL. Note that because the calculated band gap of Cs_2AuBiI_6 is quite small, it is unlikely suitable as a light-absorbing material in solar cells. Here we systematically study the structures, photoinduced carrier distribution, charge transport, and band alignment of the $Cs_2AgBiBr_6/TiO_2$, $Cs_2AgBiCl_6/TiO_2$, $Cs_2CuBiBr_6/TiO_2$, and $Cs_2CuBiCl_6/TiO_2$ heterojunctions. The aim of this study is to have a better understanding of the interfacial properties of the double perovskite-based solar devices.

2. COMPUTATIONAL METHODS

Quantum ESPRESSO package has been utilized to perform the computations.[42−44] Perdew−Burke−Ernzerhof (PBE) parametrization of the generalized gradient approximation for solid (PBEsol) was adopted to treat the exchange correlation interactions.[45] The GBRV ultrasoft pseudopotential was used to describe the interactions between valence electrons and atomic cores.[46] In Table 1, we list lattice parameters of $Cs_2AgBiBr_6$ and $CsAgBiCl_6$ based on structure optimization with PBEsol exchange functional. The computed lattice parameters are close to the experimental values (Table 1), suggesting that the selection of PBEsol exchange functional is reasonable for these systems. Although the HSE06 hybrid functional is more accurate in computing the electronic structure, the large system size of the heterostructure considered (with 148 atoms) is beyond our computing capability. To make the lattice mismatch as small as possible, $a'3 \times b'3 \times c'$ supercell of anatase TiO_2 is in contact with the double perovskite to build the interfacial heterostructure. The lattice mismatch between $Cs_2AgBiBr_6$ and $a'3 \times b'3 \times c'$ supercell of TiO_2 is merely ∼0.7%. The lattice constants for the bulk double perovskites[32,33] and TiO_2[47] are taken from the experiments. Two different surface cuttings of the double perovskites, that is, $B_2Bi_2X_8$ (B = Ag, Cu; X = Br, Cl) and Cs_4X_4 (X = Br, Cl) surfaces, are considered for building the Cs_2BBiX_6 (B = Ag, Cu; X = Br, Cl)/TiO_2 heterostructures. These interfaces will be compared with the PbI_2 and AI [A= $CH_3NH_3^+$ and $HC(NH_2)_2^+$] interfaces[40,41] in the $APbI_3$-based heterostructures. The $B_2Bi_2X_8$ (B = Ag, Cu; X = Br, Cl) and Cs_4X_4 (X = Br, Cl) surfaces can be formed in the Ag- or Cu- and Bi- and Cs-rich solution precursors, respectively. The vacuum layer of 15 Å[48,49] is adopted to minimize the interaction between the neighboring images due to the 3D periodic arrangement of the system. The heterostructures are fully optimized until the force on the ions is <0.001 Ry/au.

Table 1. Lattice Constants of Bi-Based Double Perovskites, That Is, $Cs_2AgBiBr_6$, $Cs_2AgBiCl_6$, $Cs_2CuBiBr_6$, and $Cs_2CuBiCl_6$[a]

	a (Å)	*b* (Å)	*c* (Å)	$\alpha = \beta = \gamma$ (deg)
$Cs_2AgBiBr_6$(Exp.)[33]	11.271	11.250	11.250	90
$Cs_2AgBiCl_6$(Exp.)[33]	10.777	10.777	10.777	90
$Cs_2AgBiBr_6$(Opt.)	11.169	11.169	11.169	90
$Cs_2AgBiCl_6$(Opt.)	10.655	10.655	10.655	90
$Cs_2CuBiBr_6$(Opt.)	10.895	10.895	10.895	90
$Cs_2CuBiCl_6$(Opt.)	10.366	10.366	10.366	90
TiO_2(Exp.)[47]	11.347	11.347	11.347	90

[a]Exp. and Opt. denote the experimental and optimized structures, respectively. The lattice parameters of $a'3 \times b'3 \times c'$ supercell of anatase TiO_2 are also given.

3. RESULTS AND DISCUSSION

3.1. Structures and Electronic Properties of the Cs_2BBiX_6 (B = Ag, Cu; X = Br, Cl) Double Perovskites. The optimized lattice parameters of the $Cs_2AgBiBr_6$, $Cs_2AgBiCl_6$, $Cs_2CuBiBr_6$, and $Cs_2CuBiCl_6$ are listed in Table 1. We also cite the lattice constants of $Fm\bar{3}m$ space group double perovskites from experiments, as well as anatase TiO_2, in Table 1. The rock-salt structure of the Cs_2BBiX_6 double perovskite is shown in Figure S1, where B^+(B = Ag, Cu) and Bi^{3+} alternatively occupy the octahedral center, while Cs^+ atoms stand in the center of the cuboctahedron. To describe the distribution of the photoinduced electron−hole pairs in the bismuth-based halide double perovskites, the partial charge densities of the CBM and VBM of the four double perovskites are displayed in Figure 1. The CBM stems mainly from the Bi 6p and Ag 5s or Cu 4s states, while Bi 6s and Ag 4d or Cu 3d states contribute significantly to the VBM, suggesting that the stereochemical lone pair electrons of Bi 6s orbitals play an important role in stabilization of the rock-salt perovskites, as for the $CH_3NH_3PbI_3$-like perovskites. The lone-pair behavior of Bi 6s orbitals is related to the unusual electronic and optical properties of the double perovskites, as in the case of the organolead halide hybrid perovskites, where Pb 6s plays the key role in the unusual electronic and optical properties. Moreover, the CBM of the Cl-based perovskites distributes more uniformly than the Br-based one, corresponding to a higher density of photoinduced electrons. Bi 6s, Ag 4d, Cu 3d, Br 4p, and Cl 3p orbitals contribute to the formation of holes, as indicated from the VBM charge distribution. There are some interesting similarities between the $CH_3NH_3PbI_3$-like perovskites and the rock-salt double perovskites. Cs^+ is not involved in the formation of the CBM and VBM, whereas Bi 6s and halide p orbitals constitute the VBM states. This behavior

DOI: 10.1021/acs.jpcc.7b00138
J. Phys. Chem. C 2017, 121, 4471−4480

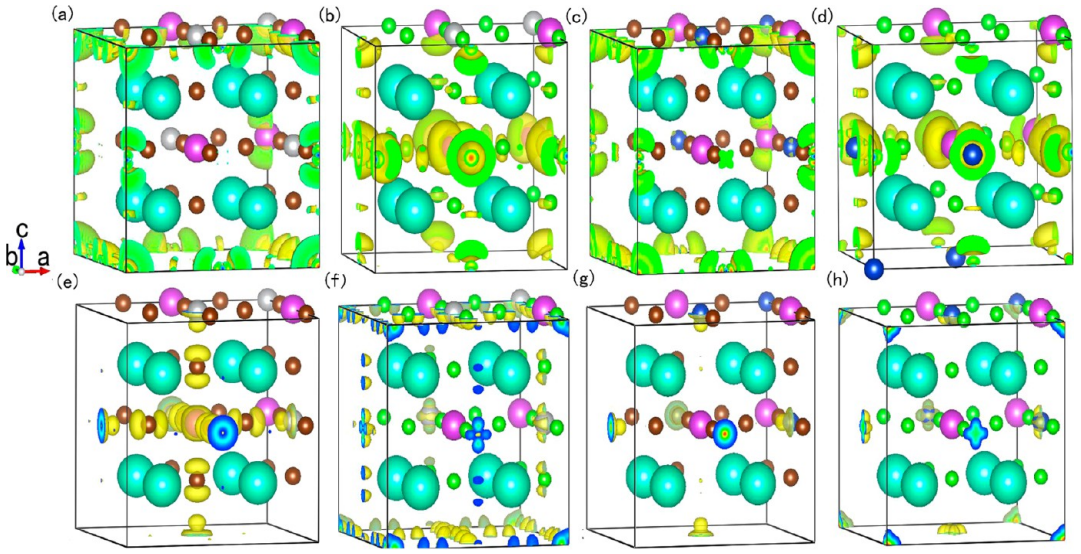

Figure 1. Partial charge density plots for the CBM of (a) $Cs_2AgBiBr_6$, (b) $Cs_2AgBiCl_6$, (c) $Cs_2CuBiBr_6$, and (d) $Cs_2CuBiCl_6$ and the VBM of (e) $Cs_2AgBiBr_6$, (f) $Cs_2AgBiCl_6$, (g) $Cs_2CuBiBr_6$, and (h) $Cs_2CuBiCl_6$.

confirms that the Bi-halide rock-salt double perovskites might be a suitable candidate as lead-free perovskites.

The effective mass (m^*) of electrons and holes is calculated by fitting the curvature of energy dispersion curve around the bottom of the conduction bands and the top of the valence bands. We use the equation $m^* = \hbar^2\left[\frac{\partial^2\varepsilon(\kappa)}{\partial\kappa^2}\right]^{-1}$ to compute the effective mass, where $\varepsilon(\kappa)$ is the band-edge eigenvalues and κ is the wave vector. The band structures of the four double perovskites are illustrated in Figure S2. The band gap and the effective mass of electrons (m_e) and holes (m_h) of the bismuth-halide double perovskite are listed in Table 2. Here we calculate

Table 2. Computed Band Gaps and Effective Masses of the Double Perovskites[a]

		effective mass			
	band gap (eV)	m_e	m_h	m_e*	m_h*
$Cs_2AgBiBr_6$	1.10	0.38	0.35	0.37[33]	0.14[33]
$Cs_2AgBiCl_6$	1.71	0.43	0.44	0.53[33]	0.15[33]
$Cs_2CuBiBr_6$	0.51	0.35	0.42		
$Cs_2CuBiCl_6$	0.83	0.47	0.56		

[a]Effective masses from ref 33 are also given. m_e and m_h denote the effective mass for electrons and holes, respectively.

m_e and m_h along L → Γ in κ space, as shown in Figure S2. Ag-based halide perovskites possess larger band gap compared with the Cu-based counterparts, while Cl-based materials exhibit larger band gap than the Br-based analogues. The Cu 3d or Ag 4d orbitals, hybridized with the Bi 6s orbitals, give rise to an indirect band gap. The largest band gap is 1.71 eV among the four structures. The smallest effective electron mass is 0.35 for $Cs_2Cu_2BiBr_6$, while the largest one is 0.47 for $Cs_2CuBiCl_6$. The smallest effective hole mass is 0.35 for $Cs_2AgBiBr_6$, for which the highest carrier mobility can be realized because of the smaller effective electron and hole masses compared with other analogues. Note that the PBEsol functional gives rise to smaller dispersion at VBM compared with the HSE06 hybrid functional, thereby leading to a larger effective hole mass than that reported in ref 33. In summary, Br-based double perovskites, that is, $Cs_2AgBiBr_6$ and $Cs_2CuBiBr_6$, are predicted to have the pronounced electron mobility owing to the smaller effective masses for the photoinduced carriers. The smaller band gaps of Cs_2CuBiX_6 (X = Br, Cl) can lead to optical absorption in a wider spectral range, making the double perovskites suitable as light-absorbing materials in optoelectronic devices.

3.2. Structures of Cs_2BBiX_6 (B = Ag, Cu; X = Br, Cl)/TiO_2 Heterojunctions. The optimized lattice parameters for the eight interfaces, that is, $B_2Bi_2X_8/TiO_2$ (B = Ag, Cu; X = Br, Cl) and Cs_4X_4/TiO_2 (X = Br, Cl) interfaces for Ag and Cu-based heterojunctions, are listed in Table 3. The bond length of the

Table 3. Lattice Parameters for the Eight Interfaces after Optimization

	a' (Å)	b' (Å)	c' (Å)	$\alpha = \beta = \gamma$ (deg)
$Ag_2Bi_2Br_8/TiO_2$ ($Cs_2AgBiBr_6/TiO_2$)	10.809	11.309	35.476	90
Cs_4Br_4/TiO_2 ($Cs_2AgBiBr_6/TiO_2$)	10.771	11.332	35.460	90
$Ag_2Bi_2Cl_8/TiO_2$ ($Cs_2AgBiCl_6/TiO_2$)	10.762	11.261	35.227	90
Cs_4Cl_4/TiO_2 ($Cs_2AgBiCl_6/TiO_2$)	10.706	11.277	35.860	90
$Cu_2Bi_2Br_8/TiO_2$ ($Cs_2CuBiBr_6/TiO_2$)	10.782	11.322	35.526	90
Cs_4Br_4/TiO_2 ($Cs_2CuBiBr_6/TiO_2$)	10.742	11.322	35.645	90
$Cu_2Bi_2Cl_8/TiO_2$ ($Cs_2CuBiCl_6/TiO_2$)	10.772	11.286	34.883	90
Cs_4Cl_4/TiO_2 ($Cs_2CuBiCl_6/TiO_2$)	10.688	11.311	35.296	90

ions in the interfaces are shown in Table S1. The atomic labels in Table S1 are drawn in Figures S3 and S4. For $B_2Bi_2X_8/TiO_2$ (B = Ag, Cu; X = Br, Cl) interfaces, the bonding length between Ag or Cu and O is shorter than that between Ag or Cu and the halide ions, indicating stronger interaction and atomic distortions across the interfaces. On the TiO_2 side, the Ti−O bonding length is shorter than that between Ti and the halide ions in perovskites, reflecting the fact that the TiO_2 is much more rigid than the double perovskites. For Cs_4X_4/TiO_2 (X =

DOI: 10.1021/acs.jpcc.7b00138
J. Phys. Chem. C 2017, 121, 4471−4480

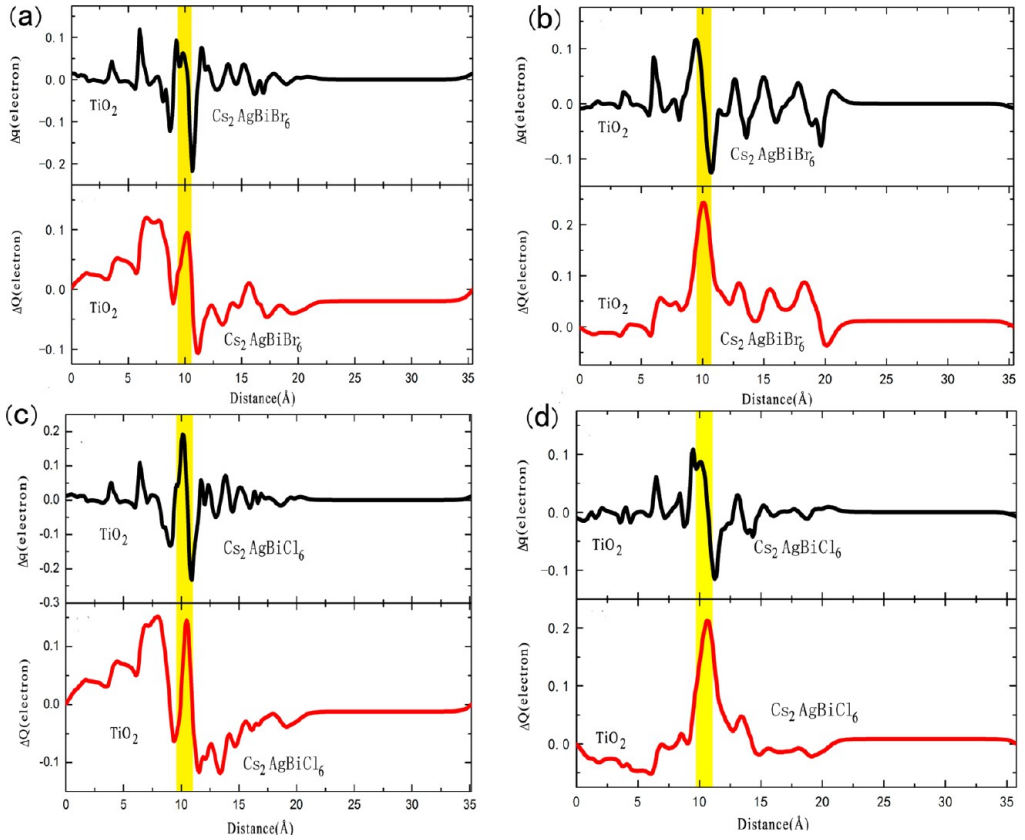

Figure 2. Plane-averaged charge difference and charge displacement curve (CDC) of (a) $Ag_2Bi_2Br_8/TiO_2$, (b) Cs_4Br_4/TiO_2, (c) $Ag_2Bi_2Cl_8/TiO_2$, and (d) Cs_4Cl_4/TiO_2 interfaces in Cs_2AgBiX_6 (X = Br and Cl)/TiO_2 heterostructures. The upper and the lower panels in (a)−(d) show the plane-averaged charge difference and the CDC, respectively.

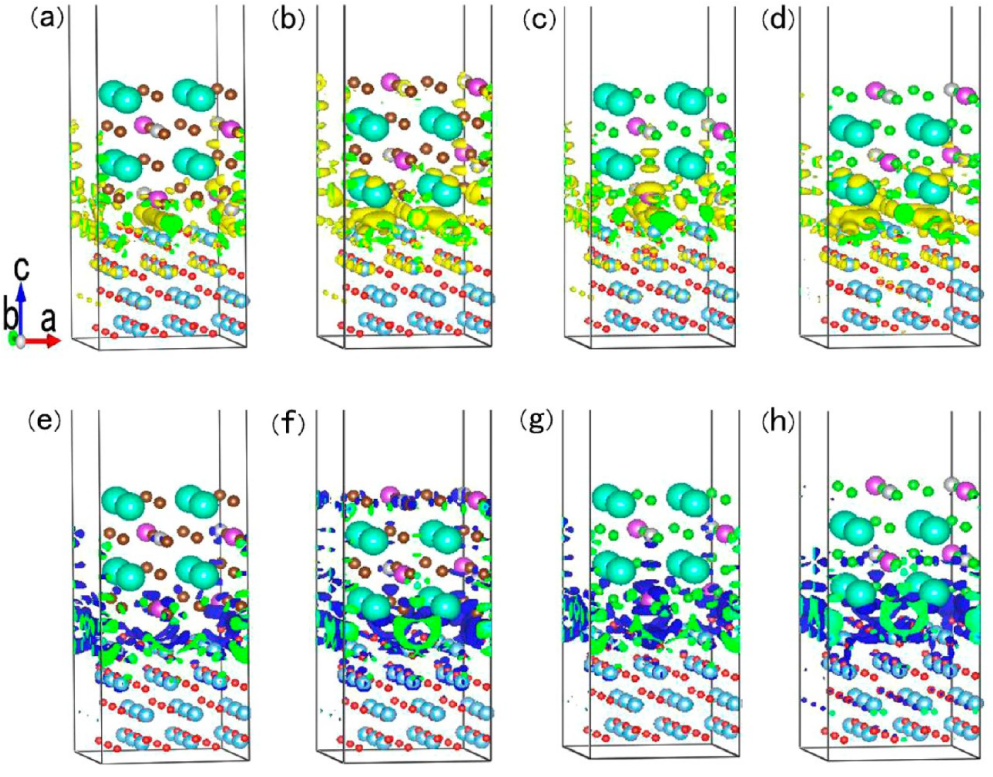

Figure 3. Charge accumulation at (a) $Ag_2Bi_2Br_8/TiO_2$, (b) Cs_4Br_4/TiO_2, (c) $Ag_2Bi_2Cl_8/TiO_2$, and (d) Cs_4Cl_4/TiO_2 interfaces and the charge depletion of (e) $Ag_2Bi_2Br_8/TiO_2$, (f) Cs_4Br_4/TiO_2, (g) $Ag_2Bi_2Cl_8/TiO_2$, and (h) Cs_4Cl_4/TiO_2 interfaces in Cs_2AgBiX_6 (X = Br and Cl)/TiO_2 heterojunctions. The charge difference is kept at 0.007 electron/$Å^3$.

DOI: 10.1021/acs.jpcc.7b00138
J. Phys. Chem. C 2017, 121, 4471−4480

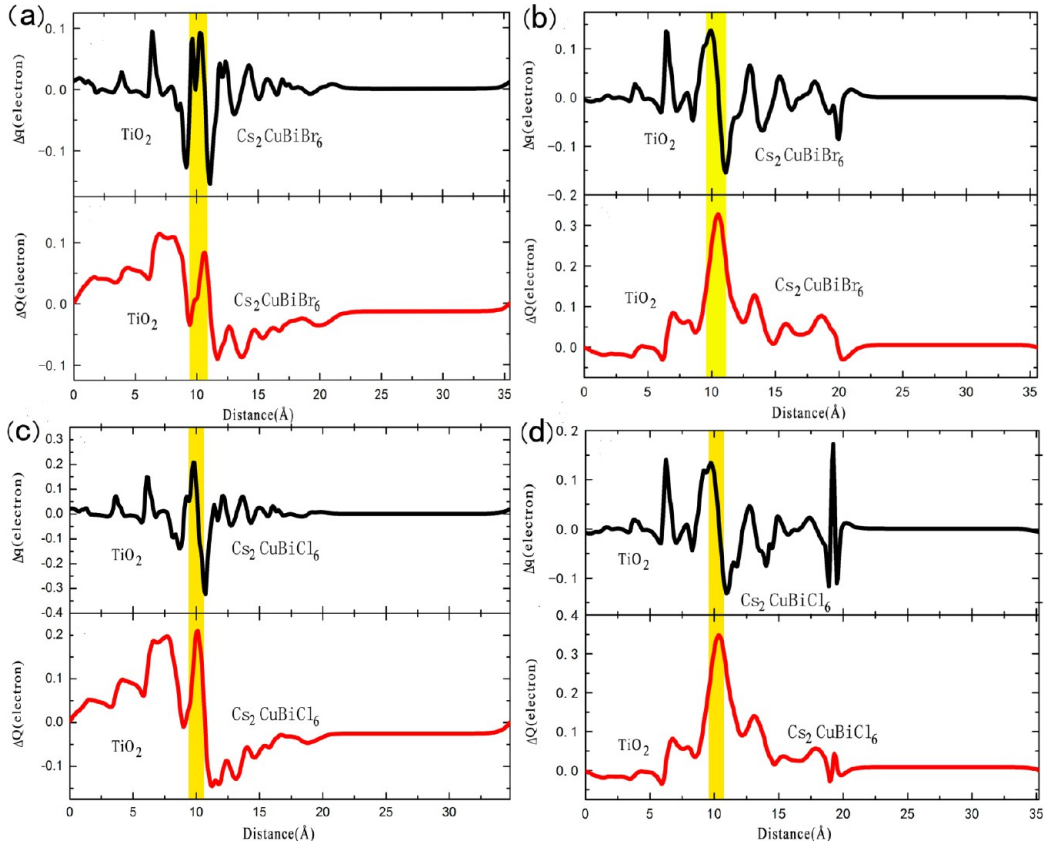

Figure 4. CDC of (a) $Cu_2Bi_2Br_8/TiO_2$, (b) Cs_4Br_4/TiO_2, (c) $Cu_2Bi_2Cl_8/TiO_2$, and (d) Cs_4Cl_4/TiO_2 interfaces in Cs_2CuBiX_6 (X = Br and Cl)/TiO_2 heterojunctions. The upper and lower panels show the plane-averaged charge difference and the CDC, respectively.

Br, Cl) interfaces in Ag- and Cu-based heterojunctions, the bonding length between Cs^+ and O^{2-} is shorter than the Cs−X (X = Br, Cl) bond length, while the Ti−O bonding length is still shorter than Ti−X (X = Br, Cl) bond length. By comparing the bonding length of anions and cations across the eight interfaces, we find that Ag, Cu, and Cs tend to bond with the oxygen of TiO_2 slab, rather than the halide ions of double perovskites slab. The bonding between the oxygen and the cations in the perovskite side takes place because of position distortion of the cations like Ag, Cu, and Cs ions in the double perovskite side, resulting in strong activity of the Bi-based rock-salt double perovskite surfaces.

3.3. Charge Transport in Cs_2BBiX_6 (B = Ag, Cu; X = Br, Cl)/TiO_2 Heterojunctions. The charge displacement curve (CDC) is a useful way for characterizing charge transport across the interfaces. The CDC across the interfaces can be computed from the charge difference between the heterojunction and two bulk components. The charge difference Δq between the heterojunction and the two components, integrated over the xy plane, has the form

$$\Delta q = \int_{-\infty}^{\infty}\int_{-\infty}^{\infty} (\rho_{Cs_2BBiX_6/TiO_2} - \rho_{Cs_2BBiX_6} - \rho_{TiO_2})\, dx\, dy \quad (1)$$

where $\rho_{Cs_2BBiX_6}$ and ρ_{TiO_2} denote charge density at Cs_2BBiX_6 and TiO_2 component of the heterojunction, respectively. The CDC, $\Delta Q(z)$, can be computed by integrating the charge difference $\Delta q(z)$ along the normal direction (z direction) to the interface

$$\Delta Q = \int_{-\infty}^{z} \Delta q\, dz \quad (2)$$

The plane-averaged charge difference and the CDC for Ag-based heterojunction, that is, $Ag_2Bi_2Br_8/TiO_2$, Cs_4Br_4/TiO_2, $Ag_2Bi_2Cl_8/TiO_2$, and Cs_4Cl_4/TiO_2 interfaces, are shown in Figure 2. The CDC of $Ag_2Bi_2Br_8/TiO_2$ and $Ag_2Bi_2Cl_8/TiO_2$ interfaces changes signs in the vicinity of the interface (marked by yellow bar in Figure 2), while the halide-based interfaces, that is, Cs_4Br_4/TiO_2 and Cs_4Cl_4/TiO_2 interfaces, give positive values over the whole heterojunctions. A positive value of the CDC at a point indicates that the charges transfer from the right to the left part across the normal plane passing through that point. The positive gradient implies that the charge is accumulating in that region while the negative gradient indicates the depletion of the charges in the corresponding region. The positive value of CDC in the whole region of the halide-based interfaces, that is, Cs_4Br_4/TiO_2 and Cs_4Cl_4/TiO_2 interfaces, shows that the charges are transported from the bismuth-based double perovskites to the TiO_2 side. Both Cs_4Br_4/TiO_2 and Cs_4Cl_4/TiO_2 interfaces seem preferable to the $Ag_2Bi_2Br_8/TiO_2$ and $Ag_2Bi_2Cl_8/TiO_2$ interfaces in terms of charge separation and transport in photovoltaic solar devices. To see the charge transfer in the interfaces more clearly, we present the charge accumulation and depletion of the four interfaces, $Ag_2Bi_2Br_8/TiO_2$, Cs_4Br_4/TiO_2, $Ag_2Bi_2Cl_8/TiO_2$, and Cs_4Cl_4/TiO_2 interfaces, respectively, in Figure 3. More charge is transported from the perovskites to TiO_2 part in Cs_4Br_4/TiO_2 and Cs_4Cl_4/TiO_2 interfaces than in $Ag_2Bi_2Br_8/TiO_2$ and $Ag_2Bi_2Cl_8/TiO_2$ interfaces, consistent with the CDC results.

To gain more insights into the charge transport in the Bi-based double perovskites, we substitute the Ag by Cu in the heterojunctions, that is, $Cs_2CuBiBr_6$ and $Cs_2CuBiCl_6$ heterojunctions. Two interfaces are constructed for each hetero-

DOI: 10.1021/acs.jpcc.7b00138
J. Phys. Chem. C 2017, 121, 4471−4480

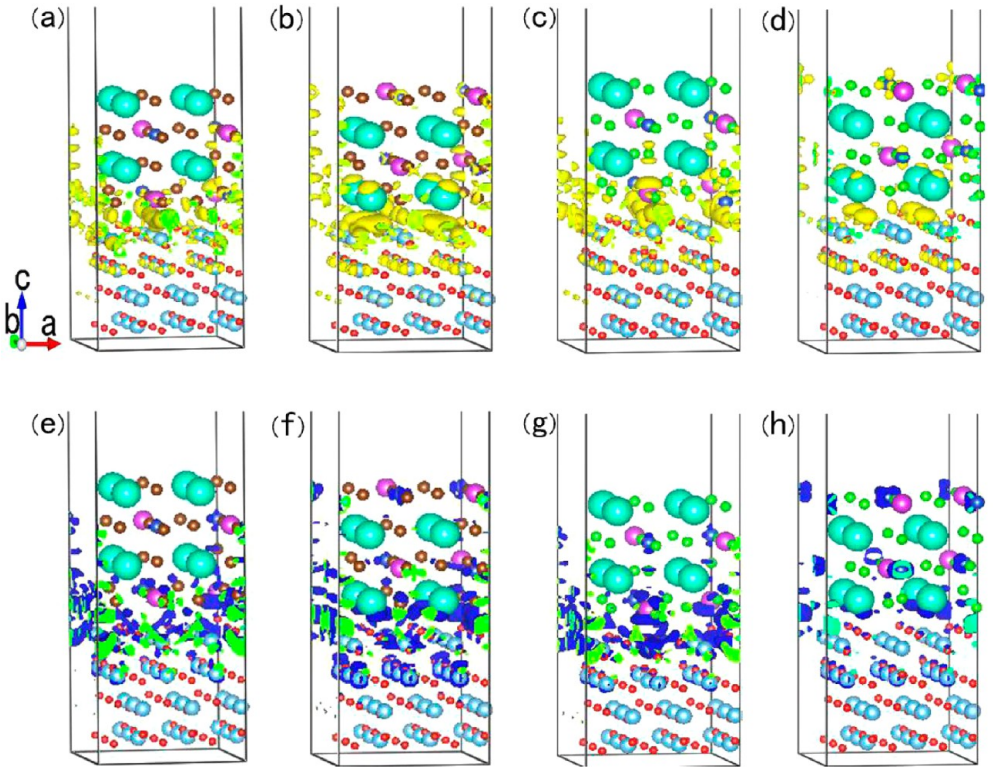

Figure 5. Charge accumulation of (a) $Cu_2Bi_2Br_8/TiO_2$, (b) Cs_4Br_4/TiO_2, (c) $Cu_2Bi_2Cl_8/TiO_2$, and (d) Cs_4Cl_4/TiO_2 interfaces and charge depletion of (e) $Cu_2Bi_2Br_8/TiO_2$, (f) Cs_4Br_4/TiO_2, (g) $Cu_2Bi_2Cl_8/TiO_2$, and (h) Cs_4Cl_4/TiO_2 interfaces in Cs_2CuBiX_6 (X = Br and Cl)/TiO_2 heterojunctions. The charge difference is kept at 0.007 electron/Å^3.

junction. Therefore, there are totally four possible interfaces for the two heterojunctions, that is, $Cu_2Bi_2Br_8/TiO_2$, Cs_4Br_4/TiO_2, $Cu_2Bi_2Cl_8/TiO_2$, and Cs_4Cl_4/TiO_2 interfaces. The CDCs of these interfaces are given in Figure 4. The charge accumulation and depletion are shown in Figure 5. For $Cs_2CuBiBr_6/TiO_2$ and $Cs_2CuBiCl_6/TiO_2$ heterojunctions, we obtain similar results that more charge transfer is seen for the halide-based interfaces, that is, Cs_4Br_4/TiO_2 and Cs_4Cl_4/TiO_2 interfaces, while the $Cu_2Bi_2Br_8/TiO_2$ and $Cu_2Bi_2Cl_8/TiO_2$ interfaces exhibit less charge transfer across the interfaces. The maximum value of CDC for Cs_4Br_4/TiO_2 and Cs_4Cl_4/TiO_2 interfaces in Cs_2CuBiX_6 (X = Br and Cl)/TiO_2 heterojunctions is 0.33 and 0.35 electrons, respectively. The transported charges across the Cs_4Br_4/TiO_2 and Cs_4Cl_4/TiO_2 interfaces for Cs_2AgBiX_6 (X = Br and Cl)/TiO_2 heterojunctions are 0.24 and 0.21 electrons, respectively. The more transported electrons across the interfaces render more transfer and separation of pronounced photoinduced electron−hole pairs and are thereby more effective for photovoltaic applications. Compared with the charge transfer in $FAPbI_3/TiO_2$ (FA = $HC(NH_2)_2^+$) heterojunction,[41] enhanced electron transfer is seen from double perovskites layer to TiO_2 layer at the Cs_4X_4/TiO_2 interfaces of Ag and Cu-based heterojunctions and thereby enhanced the separation of carriers.

To have a better understanding of the mechanism underlying the charge transfer across the interfaces, we plot the charge-density distribution, corresponding to the CBM and VBM of the Bi-based double perovskite slabs (taken directly from the optimized heterojunctions) in Figures S5 and S6, respectively. The charge density of the CBM is mainly confined in some special region of $B_2Bi_2X_8$ (B = Ag, Cu; X = Br, Cl)-terminated interface, while the photoinduced electrons are distributed uniformly over the region of Cs_4X_4 (X = Br and Cl)/TiO_2 interface, and they can penetrate deeply along the z direction, a clear indication of high density of photogenerated electrons and high charge transfer ability. There are also some trap states for the $B_2Bi_2X_8$ (B = Ag,Cu; X = Br,Cl)/TiO_2 interfaces, while for the Cs_4X_4 (X = Br and Cl)/TiO_2 interfaces the states within the band gap disappear. The band structures of the $Ag_2Bi_2Br_8$-, Cs_4Br_4-, $Ag_2Bi_2Cl_8$-, and Cs_4Cl_4-terminated slabs, and the corresponding TiO_2 slabs taken from the optimized $Cs_2Ag_2BiBr_6/TiO_2$ and $Cs_2Ag_2BiCl_6/TiO_2$ heterojunctions are given in Figures S7 and S8, respectively. The trap states due to the TiO_2 part for the $Ag_2Bi_2X_8$ (X = Br and Cl)/TiO_2 interfaces hinder the charge transfer and separation. These trap states stem mainly from the 2p states of position-distorted oxygen atoms of TiO_2 in the interfacial region due to the stronger chemical bonding with the metal ions in the double perovskite side. It is interesting to see that no band gap states exist from the TiO_2 side of Cs_4X_4 (X = Br and Cl)/TiO_2 interfaces, which is consistent with the pronounced charge transfer and the smooth charge pathway across the Cs_4X_4 (X = Br and Cl) terminations.

3.4. Electronic Characteristics for Cs_2BBiX_6 (B = Ag, Cu; X = Br, Cl)/TiO_2 Heterojunctions. To elucidate the charge flow pathway in the interfaces, we plot in Figures 6 and 7 the locally projected density of states (PDOS) in the normal direction to the Ag- and Cu-based bismuth double perovskite interfaces, respectively. The qualitative band alignment, for example, the relatively higher conduction band energy level of Cs_2BBiX_6 (B = Ag, Cu; X = Br, Cl) over that of TiO_2 is seen for all heterojunctions, implying either interface charge extraction or electrons injection. For the $Ag_2Bi_2Br_8/TiO_2$ interfaces in the $Cs_2AgBiBr_6/TiO_2$ heterojunction, large densities of states

DOI: 10.1021/acs.jpcc.7b00138
J. Phys. Chem. C 2017, 121, 4471−4480

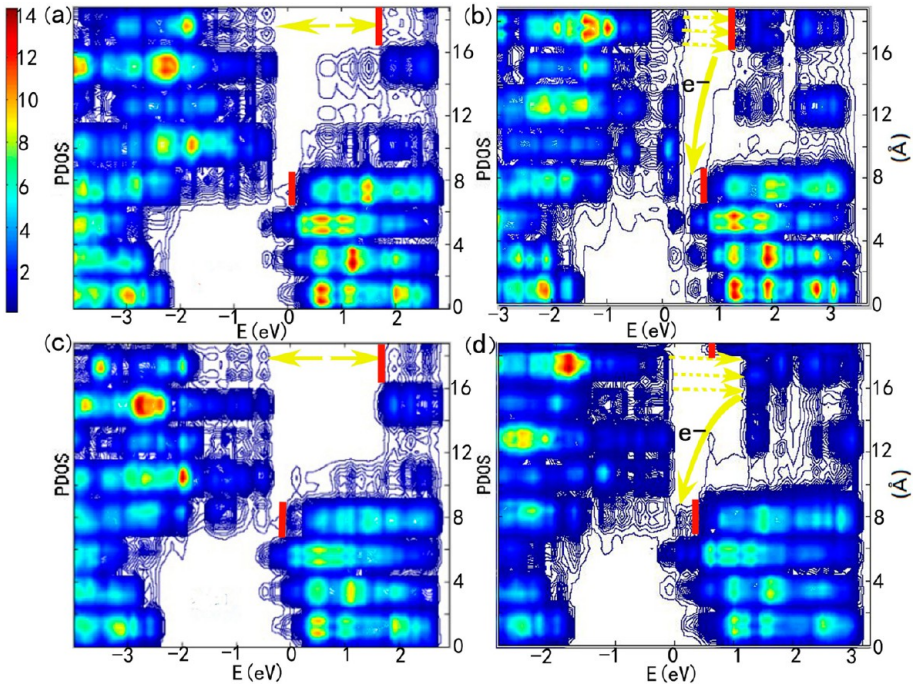

Figure 6. Locally projected DOS along the normal direction (z direction) to (a) $Ag_2Bi_2Br_8/TiO_2$, (b) Cs_4Br_4/TiO_2, (c) $Ag_2Bi_2Cl_8/TiO_2$, and (d) Cs_4Cl_4/TiO_2 interfaces in the Cs_2AgBiX_6 (X = Br and Cl)/TiO_2 heterojunctions. The solid yellow arrows mark charge extraction. The yellow dashed arrows denote possible optical transition (absorption) within the band gap in perovskites side. The upper and lower red bars denote the CBMs for Cs_2AgBiX_6 (X = Br and Cl) and TiO_2.

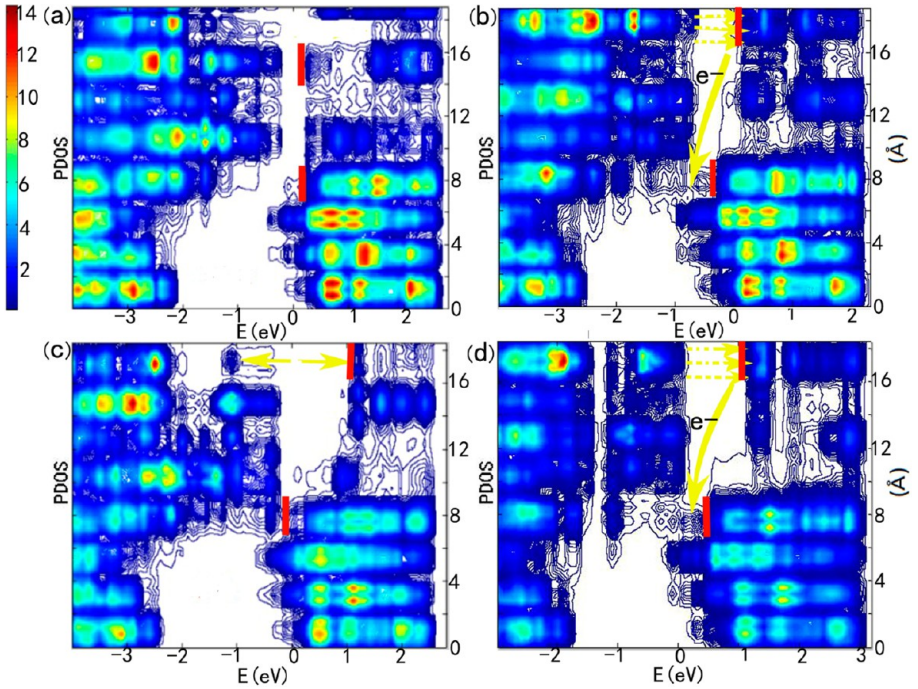

Figure 7. Locally projected DOS along the normal direction (z direction) to (a) $Cu_2Bi_2Br_8/TiO_2$, (b) Cs_4Br_4/TiO_2, (c) $Cu_2Bi_2Cl_8/TiO_2$, and (d) Cs_4Cl_4/TiO_2 interfaces in the Cs_2CuBiX_6 (X = Br and Cl)/TiO_2 heterojunctions. The solid yellow arrows mark charge extraction. The yellow dashed arrows denote possible optical transition (absorption) within the band gap in perovskites side. The upper and lower vertical red bars denote the CBMs for Cs_2CuBiX_6 (X = Br and Cl) and TiO_2.

(DOS) above the CBM of $Cs_2AgBiBr_6$ are seen, which are positioned about 1.6 eV higher than the conduction band edge of TiO_2 (see Figure 6a, the energy difference between two vertical red bars) while the double perovskite conduction band edge extends further to the same level as the TiO_2 with less DOS distributed at the bottom region. For the Cs_4Br_4/TiO_2 interfaces in the $Cs_2AgBiBr_6/TiO_2$ heterojunction, the energy barrier between the conduction band edge of $Cs_2AgBiBr_6$ and TiO_2 (see the energy difference between two red bars in Figure 6b) as well as the band gap of the double perovskite decreases,

DOI: 10.1021/acs.jpcc.7b00138
J. Phys. Chem. C 2017, 121, 4471−4480

facilitating absorption of light and charge transfer from the perovskite to the ETL, that is, the TiO_2 side, leading to pronounced photogenerated electron−hole pair extraction and separation. This result can account well for the charge-transfer effect in Cs_4Br_4/TiO_2 interfaces from the CDC and the charge accumulation and depletion analysis shown in Figures 2 and 3, respectively. For $Ag_2Bi_2Cl_8/TiO_2$ and Cs_4Cl_4/TiO_2 interfaces in $Cs_2AgBiCl_6$ heterojunction, the band alignment and the charge flow pathway are seen from the distribution of local PDOS of $Cs_2AgBiCl_6$ and TiO_2 (see Figure 6). The difference of the major PDOS for the conduction band of the two components for the $Ag_2Bi_2Cl_8/TiO_2$ interface increases further, which hinders the photogenerated electrons passing from the light absorber, that is, $Cs_2AgBiCl_6$, to the ETL side. It is worth mentioning that the band gap of the $Cs_2AgBiCl_6$ decreases when combined with TiO_2 at the Cs_4Cl_4/TiO_2 interface, as in the case of $Cs_2AgBiBr_6/TiO_2$ heterojunction with Cs_4Br_4/TiO_2 interface. The reduced band gap of the double perovskite extends the light absorption from the visible light to the infrared region, making this rock-salt perovskite a good light absorber. We take the band gap of the double perovskites several layers away from the contact interface. Therefore, the band gap is more for bulk than for just the interface. The band gap is bigger than the energy difference between the CBM of the double perovskites and TiO_2. As the photon is absorbed, the valence band electron will be excited to the conduction band, and the carrier will flow easily from the conduction band of the double perovskites to the conduction band of TiO_2 rather than come back to the valence band. Moreover, the enhanced photoinduced electrons can flow from the perovskite to TiO_2 side smoothly due to the gradient distribution of PDOS at perovskite side and the small energy barrier between the CBM of the rock-salt perovskite and TiO_2.

The Cu-based analogs exhibit similar electronic characteristics as the Cs_2AgBiX_6 (X = Br, Cl)-based heterojunctions (see Figure 7). The energy difference between the dominant states in conduction band and valence band of perovskites is decreased in Cs_4Cl_4/TiO_2-mediated interfaces, as compared with that of $Cu_2Bi_2Cl_8/TiO_2$ interfaces. The conduction band edge of $Cs_2CuBiBr_6$ is located approximately at the same level as TiO_2 for the $Cu_2Bi_2Br_8/TiO_2$-mediated interface. Some states in the vicinity of the CBM of double perovskites are at an even lower energy level than that of TiO_2, which hinders photoinduced electron transfer across the interface. The smooth extension of the locally PDOS at the $Cs_2CuBiBr_6$ or $Cs_2CuBiCl_6$ side with Cs_4Br_4/TiO_2- and Cs_4Cl_4/TiO_2-mediated interfaces where the gradient distribution of PDOS decreases from the double perovskite to TiO_2 side is good for photoinduced charge extraction and separation. For $Cs_2CuBiCl_6/TiO_2$ heterojunction, the $Cu_2Bi_2Cl_8/TiO_2$-mediated interface results in a relatively wider band gap than the Cs_4Cl_4/TiO_2 interface, hampering the photon absorption in the perovskite. $Cs_2CuBiBr_6$- and $Cs_2CuBiCl_6$-based heterojunctions exhibit a decreased band gap in the perovskite side compared with $Cs_2AgBiBr_6$- and $Cs_2AgBiCl_6$-based heterojunctions due mainly to the intrinsic electronic properties of the double perovskites rather than the interfacial effect. It is worth mentioning that the band alignment between $Cs_2CuBiBr_6$ and TiO_2 with the $Cu_2Bi_2Br_8/TiO_2$-mediated interface is not feasible for charge transfer across the interfaces. Fortunately, the lowered energy difference between the dominant DOS in the conduction band and the valence band is still seen, which can be attributed to the interfacial effect (Cs_4Cl_4/TiO_2-mediated interfaces). The appropriate band gap and band alignment for Cs_4Br_4/TiO_2- and Cs_4Cl_4/TiO_2-mediated interfaces together with the gradient distribution of conduction band edge over the perovskite side enable efficient charge extraction for possible interface engineering of solar cells.

4. CONCLUSIONS

Motivated by the recent successful synthesis of Pb-free $Cs_2AgBiBr_6$ and $Cs_2AgBiCl_6$ double perovskites, we have investigated the structure and the charge transfer properties in the Cs_2BBiX_6 (B = Ag,Cu; X = Br,Cl)/TiO_2 heterojunctions on the basis of DFT computations. We found that Cs, Ag, and Bi tend to bond with the oxygen from TiO_2 side with a shorter bond length compared with that of metal-halide ions. From the CDC analysis, we found pronounced charge transfer from the double perovskite side to TiO_2 side for the Cs_4X_4 (X = Br and Cl)-/TiO_2-mediated interfaces, while the $B_2Bi_2X_8$ (B = Ag,Cu; X = Br,Cl)/TiO_2 interfaces do not give continuous charge transfer across the interfaces. We also analyzed the locally projected DOS of the two components in the normal direction to the interfaces and identified the band alignment and charge extraction across the interfaces. A clear charge flow pathway is seen for the Cs_4X_4 (X = Br and Cl)/TiO_2-mediated interfaces with a reduced band gap in double perovskite side, together with a lower energy barrier between the bottom of conduction band of Cs_2BBiX_6 (B = Ag,Cu; X = Br,Cl) and TiO_2. Meanwhile, the reduced band gap and gradient distribution of PDOS from perovskite side can facilitate the photo absorption and charge transfer/separation. The theoretical calculations provide a better understanding of the mechanism underlying in the interfacial effect of double perovskite-based lead-free photovoltaics and suggest high potential for interfacial engineering optoelectronic devices.

■ ASSOCIATED CONTENT

Supporting Information

The Supporting Information is available free of charge on the ACS Publications website at DOI: 10.1021/acs.jpcc.7b00138.

Crystal structures of $Cs_2AgBiBr_6$ (B = Ag,Cu; X = Br,Cl); computed band structures of $Cs_2AgBiBr_6$ (B = Ag,Cu; X = Br,Cl); interfacial structures with labeled atoms and bonding for the eight interfaces; distribution of CBM and VBM of the eight interfaces in Cs_2BBiX_6 (B = Ag,Cu; X = Br,Cl)/TiO_2 heterojunctions; and computed band structures of the perovskites and TiO_2 slabs taken from Cs_2AgBiX_6 (X = Br,Cl)/TiO_2 heterojunctions. (PDF)

■ AUTHOR INFORMATION

Corresponding Authors

*H.-J.F.: E-mail: hjfeng@nwu.edu.cn.

*X.C.Z.: E-mail: xzeng1@unl.edu.

ORCID

Jinsong Huang: 0000-0002-0509-8778

Xiao Cheng Zeng: 0000-0003-4672-8585

Notes

The authors declare no competing financial interest.

■ ACKNOWLEDGMENTS

We acknowledge helpful discussions with Dr. Jun Dai and Dr. Minggang Ju. H.-J. F. was financially supported by the National Natural Science Foundation of China (NSFC) under Grant

DOI: 10.1021/acs.jpcc.7b00138
J. Phys. Chem. C 2017, 121, 4471−4480

No. 51672214, No. 11304248, and No. 11247230, the Natural Science Basic Research Plan in Shaanxi Province of China (Program No. 2014JM1014), the Scientific Research Program Funded by Shaanxi Provincial Education Department (Program No. 2013JK0624), the Fund Program for the Scientific Activities of Selected Returned Overseas Professionals in Shaanxi Province of China, and Youth Bai-Ren (100 Talents Plan) Project in Shaanxi Province of China. X.C.Z. and J.H. were supported by the National Science Foundation (NSF) through the Nebraska Materials Research Science and Engineering Center (MRSEC) (Grant No. DMR-1420645) and an NSF EPSCoR Track 2 grant (OIA-1538893).

REFERENCES

(1) Stoumpos, C. C.; Malliakas, C. D.; Kanatzidis, M. G. Semiconducting Tin and Lead Iodide Perovskites with Organic Cations: Phase Transitions, High Mobilities, and Near-Infrared Photoluminescent Properties. *Inorg. Chem.* **2013**, *52*, 9019−9038.

(2) Kojima, A.; Teshima, K.; Shirai, Y.; Miyasaka, T. Organometal Halide Perovskites as Visible-Light Sensitizers for Photovoltaic Cells. *J. Am. Chem. Soc.* **2009**, *131*, 6050−6051.

(3) McGehee, M. D. Perovskite Solar Cells: Continuing to Soar. *Nat. Mater.* **2014**, *13*, 845−846.

(4) Lee, M. M.; Teuscher, J.; Miyasaka, T.; Murakami, T. N.; Snaith, H. J. Efficient Hybrid Solar Cells Based on Meso-Superstructured Organometal Halide Perovskites. *Science* **2012**, *338*, 643−647.

(5) Dong, Q.; Fang, Y.; Shao, Y.; Mulligan, P.; Qiu, J.; Cao, L.; Huang, J. Solar cells. Electron-Hole Diffusion Lengths > 175 μm in Solution-Grown $CH_3NH_3PbI_3$ Single Crystals. *Science* **2015**, *347*, 967−970.

(6) Zhumekenov, A. A.; Saidaminov, M. I.; Haque, M. A.; Alarousu, E.; Sarmah, S. P.; Murali, B.; Dursun, I.; Miao, X.-H.; Abdelhady, A. L.; Wu, T.; et al. Formamidinium Lead Halide Perovskite Crystal with Unprecedented Long Carrier Dynamics and Diffusion Length. *ACS Energy Lett.* **2016**, *1*, 32−37.

(7) Stranks, S. D.; Eperon, G. E.; Grancini, G.; Menelaou, C.; Alcocer, M. J.; Leijtens, T.; Herz, L. M.; Petrozza, A.; Snaith, H. J. Electron-Hole Diffusion Lengths Exceeding 1 Micrometer in an Organometal Trihalide Perovskite Absorber. *Science* **2013**, *342*, 341−344.

(8) Wehrenfennig, C.; Eperon, G. E.; Johnston, M. B.; Snaith, H. J.; Herz, L. M. High Charge Carrier Mobilities and Lifetimes in Organolead Trihalide Perovskites. *Adv. Mater.* **2014**, *26*, 1584−1589.

(9) Pazos-Outón, L. M.; Szumilo, M.; Lamboll, R.; Richter, J. M.; Crespo-Quesada, M.; Abdi-Jalebi, M.; Beeson, H. J.; Vrućinić, M.; Alsari, M.; Snaith, H. J.; et al. Photon Recycling in Lead Iodide Perovskite Solar Cells. *Science* **2016**, *351*, 1430−1433.

(10) Saliba, M.; Zhang, W.; Burlakov, V. M.; Stranks, S. D.; Sun, Y.; Ball, J. M.; Johnston, M. B.; Goriely, A.; Wiesner, U.; Snaith, H. J. Plasmonic-Induced Photon Recycling in Metal Halide Perovskite Solar Cells. *Adv. Funct. Mater.* **2015**, *25*, 5038−5046.

(11) Wehrenfennig, C.; Liu, M.; Snaith, H. J.; Johnston, M. B.; Herz, L. M. Charge-Carrier Dynamics in Vapour-Deposited Films of the Organolead Halide Perovskite $CH_3NH_3PbI_{3-x}Cl_x$. *Energy Environ. Sci.* **2014**, *7*, 2269−2275.

(12) Brenner, T. M.; Egger, D. A.; Rappe, A. M.; Kronik, L.; Hodes, G.; Cahen, D. Are Mobilities in Hybrid Organic−Inorganic Halide Perovskites Actually "High"? *J. Phys. Chem. Lett.* **2015**, *6*, 4754−4757.

(13) Oga, H.; Saeki, A.; Ogomi, Y.; Hayase, S.; Seki, S. Correction to Improved Understanding of the Electronic and Energetic Landscapes of Perovskite Solar Cells: High Local Charge Carrier Mobility, Reduced Recombination, and Extremely Shallow Traps. *J. Am. Chem. Soc.* **2014**, *136*, 13818−13825.

(14) Zhu, X.-Y.; Podzorov, V. Charge Carriers in Hybrid Organic−Inorganic Lead Halide Perovskites Might be Protected as Large Polarons. *J. Phys. Chem. Lett.* **2015**, *6*, 4758−4761.

(15) Jellicoe, T. C.; Richter, J. M.; Glass, H. F.; Tabachnyk, M.; Brady, R.; Dutton, S. E.; Rao, A.; Friend, R. H.; Credgington, D.; Greenham, N. C.; et al. Synthesis and Optical Properties of Lead-Free Cesium Tin Halide Perovskite Nanocrystals. *J. Am. Chem. Soc.* **2016**, *138*, 2941−2944.

(16) Boix, P. P.; Agarwala, S.; Koh, T. M.; Mathews, N.; Mhaisalkar, S. G. Perovskite Solar Cells: Beyond Methylammonium Lead Iodide. *J. Phys. Chem. Lett.* **2015**, *6*, 898−907.

(17) Lai, M. L.; Tay, T. Y. S.; Sadhanala, A.; Dutton, S. E.; Li, G.; Friend, R. H.; Tan, Z.-K. Tunable Near-Infrared Luminescence in Tin Halide Perovskite Devices. *J. Phys. Chem. Lett.* **2016**, *7*, 2653−2658.

(18) Braly, I. L.; Hillhouse, H. W. Optoelectronic Quality and Stability of Hybrid Perovskites from $MAPbI_3$ to $MaPbI_2Br$ Using Composition Spread Libraries. *J. Phys. Chem. C* **2016**, *120*, 893−902.

(19) Manser, J. S.; Saidaminov, M. I.; Christians, J. A.; Bakr, O. M.; Kamat, P. V. Making and Breaking of Lead Halide Perovskites. *Acc. Chem. Res.* **2016**, *49*, 330−338.

(20) Naresh, G.; Mandal, T. K. Excellent Sun-Light-Driven Photocatalytic Activity by Aurivillius Layered Perovskites, $Bi_{5-x}La_xTi_3FeO_{15}$ (x= 1, 2). *ACS Appl. Mater. Interfaces* **2014**, *6*, 21000−21010.

(21) Sun, Y.-Y.; Agiorgousis, M. L.; Zhang, P.; Zhang, S. Chalcogenide Perovskites for Photovoltaics. *Nano Lett.* **2015**, *15*, 581−585.

(22) Hu, L.; Shao, G.; Jiang, T.; Li, D.; Lv, X.; Wang, H.; Liu, X.; Song, H.; Tang, J.; Liu, H. Investigation of the Interaction Between Perovskite Films with Moisture via in Situ Electrical Resisitance Measurement. *ACS Appl. Mater. Interfaces* **2015**, *7*, 25113−25120.

(23) Green, M. A.; Jiang, Y.; Soufiani, A. M.; Ho-Baillie, A. Optical Properties of Photovoltaic Organic-Inorganic Lead Halide Perovskites. *J. Phys. Chem. Lett.* **2015**, *6*, 4774−4785.

(24) Cao, D. H.; Stoumpos, C. C.; Farha, O. K.; Hupp, J. T.; Kanatzidis, M. G. 2D Homologous Perovskites as Light-Absorbing Materials for Solar Cell Applications. *J. Am. Chem. Soc.* **2015**, *137*, 7843−7850.

(25) Dou, L.; Wong, A. B.; Yu, Y.; Lai, M.; Kornienko, N.; Eaton, S. W.; Fu, A.; Bischak, C. G.; Ma, J.; Ding, T.; et al. Atomically Thin Two-Dimensional Organic-Inorganic Hybrid Perovskites. *Science* **2015**, *349*, 1518−1521.

(26) Fang, H.; Jena, P. Super-Ion Inspired Colorful Hybrid Perovskite Solar Cells. *J. Mater. Chem. A* **2016**, *4*, 4728−4737.

(27) Fang, H.; Jena, P. Molecular Origin of Properties of Organic-Inorganic Hybrid Perovskites: The Big Picture from Small Clusters. *J. Phys. Chem. Lett.* **2016**, *7*, 1596−1603.

(28) Yao, Q.; Fang, H.; Deng, K.; Kan, E.; Jena, P. Superhalogens as Building Blocks of Two-Dimensional Organic-inorganic Hybrid Perovskites for Optoelectronics Applications. *Nanoscale* **2016**, *8*, 17836−17842.

(29) Beal, R. E.; Slotcavage, D. J.; Leijtens, T.; Bowring, A. R.; Belisle, R. A.; Nguyen, W. H.; Burkhard, G. F.; Hoke, E. T.; McGehee, M. D. Cesium Lead Halide Perovskites with Improved Stability for Tandem Solar Cells. *J. Phys. Chem. Lett.* **2016**, *7*, 746−751.

(30) Yantara, N.; Bhaumik, S.; Yan, F.; Sabba, D.; Dewi, H. A.; Mathews, N.; Boix, P. P.; Demir, H. V.; Mhaisalkar, S. Inorganic Halide Perovskites for Efficient Light-Emitting Diodes. *J. Phys. Chem. Lett.* **2015**, *6*, 4360−4364.

(31) Ohmann, R.; Ono, L. K.; Kim, H.-S.; Lin, H.; Lee, M. V.; Li, Y.; Park, N.-G.; Qi, Y. Real-Space Imaging of the Atomic Structure of Organic-Inorganic Perovskite. *J. Am. Chem. Soc.* **2015**, *137*, 16049−16054.

(32) Slavney, A.; Hu, T.; Lindenberg, A. M.; Karunadasa, H. I. A Bismuth-Halide Double Perovskite with Long Carrier Recombination Lifetime for Photovoltaic Applications. *J. Am. Chem. Soc.* **2016**, *138*, 2138−2141.

(33) McClure, E. T.; Ball, M. R.; Windl, W.; Woodward, P. M. Cs_2AgBiX_6 (X = Br, Cl): New Visible Light Absorbing, Lead-Free Halide Perovskite Semiconductors. *Chem. Mater.* **2016**, *28*, 1348−1354.

(34) Filip, M. R.; Hillman, S.; Haghighirad, A. A.; Snaith, H. J.; Giustino, F. Band Gaps of the Lead-Free Halide Double Perovskites

DOI: 10.1021/acs.jpcc.7b00138
J. Phys. Chem. C 2017, 121, 4471−4480

$Cs_2BiAgCl_6$ and $Cs_2BiAgBr_6$ from Theory and Experiment. *J. Phys. Chem. Lett.* **2016**, *7*, 2579−2585.
(35) Deng, Z.; Wei, F.; Sun, S.; Kieslich, G.; Cheetham, A. K.; Bristowe, P. D. Exploring the Properties of Lead-Free Hybrid Double Perovskites Using a Combined Computational-Experimental Approach. *J. Mater. Chem. A* **2016**, *4*, 12025−12029.
(36) Han, G. S.; Song, Y. H.; Jin, Y. U.; Lee, J.-W.; Park, N.-G.; Kang, B. K.; Lee, J.-K.; Cho, I. S.; Yoon, D. H.; Jung, H. S. Reduced Graphene Oxide/Mesoporous TiO_2 Nanocomposite Based Perovskite Solar Cells. *ACS Appl. Mater. Interfaces* **2015**, *7*, 23521−23526.
(37) Foley, B. J.; Marlowe, D. L.; Sun, K.; Saidi, W. A.; Scudiero, L.; Gupta, M. C.; Choi, J. J. Temperature Dependent Energy Levels of Methylammonium Lead Iodide Perovskite. *Appl. Phys. Lett.* **2015**, *106*, 243904.
(38) Fabregat-Santiago, F.; Bisquert, J.; Cevey, L.; Chen, P.; Wang, M.; Zakeeruddin, S. M.; Grätzel, M. Electron Transport and Recombination in Solid-State Dye Solar Cell with Spiro-Ometad as Hole Conductor. *J. Am. Chem. Soc.* **2009**, *131*, 558−562.
(39) Noh, J.; Jeon, N.; Choi, Y.; Nazeeruddin, M. K.; Gratzel, M.; Seok, S. Nanostructured $TiO_2/CH_3NH_3PbI_3$ Heterojunction Solar Cells Employing Spiro-Ometad/Co-Complex as Hole-Transporting Material. *J. Mater. Chem. A* **2013**, *1*, 11842−11847.
(40) Feng, H.-J.; Paudel, T. R.; Tsymbal, E. Y.; Zeng, X. C. Tunable Optical Properties and Charge Separation in $CH_3NH_3Sn_{(x)}Pb_{(1-x)}I_3/TiO_2$-Based Planar Perovskites Cells. *J. Am. Chem. Soc.* **2015**, *137*, 8227−8236.
(41) Feng, H.-J.; Huang, J.; Zeng, X. C. Photovoltaic Diode Effect Induced by Positive Bias Poling of Organic Layer-Mediated Interface in Perovskite Heterostructure α-$HC(NH_2)_2PbI_3/TiO_2$. *Adv. Mater. Interfaces* **2016**, *3*, 1600267.
(42) Giannozzi, P.; Baroni, S.; Bonini, N.; Calandra, M.; Car, R.; Cavazzoni, C.; Ceresoli, D.; Chiarotti, G. L.; Cococcioni, M.; Dabo, I.; et al. QUANTUM ESPRESSO: A Modular and Open-Source Software Project for Quantum Simulations of Materials. *J. Phys.: Condens. Matter* **2009**, *21*, 395502.
(43) Walker, B.; Saitta, A. M.; Gebauer, R.; Baroni, S. Efficient Approach to Time-Dependent Density-Functional Perturbation Theory for Optical Spectroscopy. *Phys. Rev. Lett.* **2006**, *96*, 113001.
(44) Rocca, D.; Gebauer, R.; Saad, Y.; Baroni, S. Turbo Charging Time-Dependent Density-Functional Theory with Lanczos Chains. *J. Chem. Phys.* **2008**, *128*, 154105.
(45) Perdew, J. P.; Ruzsinszky, A.; Csonka, G. I.; Vydrov, O. A.; Scuseria, G. E.; Constantin, L. A.; Zhou, X.; Burke, K. Restoring the Density-Gradient Expansion for Exchange in Solids and Surfaces. *Phys. Rev. Lett.* **2008**, *100*, 136406.
(46) Garrity, K. F.; Bennett, J. W.; Rabe, K. M.; Vanderbilt, D. Pseudopotentials for High-Throughput DFT Calculations. *Comput. Mater. Sci.* **2014**, *81*, 446−452.
(47) Burdett, J. K.; Hughbanks, T.; Miller, G. J.; Richardson, J. W.; Smith, J. V. Structural-Electronic Relationships in Inorganic Solids: Powder Neutron Diffraction Studies of the Rutile and Anatase Polymorphs of Titanium Dioxide at 15 and 295 k. *J. Am. Chem. Soc.* **1987**, *109*, 3639−3646.
(48) Zhang, L.; Sit, H. L. *J.* Ab Initio Study of Interaction of Water, Hydroxyl Radicals, and Hydroxide Ions with $CH_3NH_3PbI_3$ and $CH_3NH_3PbBr_3$ Surfaces. *J. Phys. Chem. C* **2015**, *119*, 22370−22378.
(49) Wei, H.; Luo, J.-W.; Li, S.-S.; Wang, L.-W. Revealing the Origin of Fast Electron Transfer in TiO_2-Based Dye-Sensitized Solar Cells. *J. Am. Chem. Soc.* **2016**, *138*, 8165−8174.

DOI: 10.1021/acs.jpcc.7b00138
J. Phys. Chem. C 2017, 121, 4471−4480